



IJRASET

International Journal For Research in
Applied Science and Engineering Technology



INTERNATIONAL JOURNAL FOR RESEARCH

IN APPLIED SCIENCE & ENGINEERING TECHNOLOGY

Volume: 14 **Issue:** VII **Month of publication:** July 2026

DOI: <https://doi.org/10.22214/ijraset.2026.84153>

www.ijraset.com

Call:  08813907089

E-mail ID: ijraset@gmail.com

Intelligent Grid-Connected Photovoltaic Energy Management through Hybrid Storage Regulation

Ch. Vineeth¹, Dr. T. Sudhakar Babu²

¹M.E PSPE, CBIT, Hyderabad

²Associate Professor Dept. of EEE, CBIT, Hyderabad

Abstract: *The increasing penetration of solar photovoltaic (PV) generation into modern distribution networks introduces significant power-quality and stability challenges, primarily due to the intermittent nature of solar irradiance and sudden load disturbances. Conventional proportional–integral (PI) controlled PV systems supported only by battery storage respond slowly to fast transients, resulting in deep voltage sags, large voltage swells, prolonged settling times, and high total harmonic distortion (THD). This paper proposes a Model Predictive Control (MPC) based energy-management scheme for a grid-connected hybrid PV system that combines a battery energy storage system (BESS) with a supercapacitor energy storage system (SCES) on a common hybrid DC bus. The MPC controller receives the DC-link voltage reference, measured DC-link voltage, grid current, load power, battery and supercapacitor states of charge, and a predictive disturbance signal derived from irradiance, load, and grid-voltage sensors; it generates optimal gate signals for the boost converter and the three-phase inverter together with battery and supercapacitor power references. The complete system is modeled and simulated in MATLAB/Simulink and benchmarked against an existing PI-controlled PV–battery system. Simulation results demonstrate that the proposed MPC scheme limits the voltage sag to 400 V compared with 250 V for the PI system, restricts the voltage swell to 405 V against 550 V, achieves near-instantaneous settling to the 400 V steady state, and reduces the output-voltage THD from 8.5% to 2.1%, comfortably satisfying the IEEE Std. 519 limit of 5%. The frequency-decoupled power sharing between the battery and the supercapacitor further reduces battery stress and improves the overall reliability and lifetime of the storage system.*

Index Terms: *Model predictive control, solar photovoltaic, hybrid energy storage, battery, supercapacitor, DC-link voltage regulation, total harmonic distortion, voltage sag, voltage swell, power quality, MATLAB/Simulink.*

I. INTRODUCTION

The global transition toward carbon-neutral electricity has made solar photovoltaic (PV) generation one of the fastest growing renewable energy sources. However, the power output of a PV array is a strongly nonlinear function of solar irradiance and cell temperature, both of which vary rapidly with passing clouds and ambient conditions. When such an intermittent source is interfaced to the utility grid through power-electronic converters, any sudden change in irradiance or in the connected load is reflected directly on the DC-link and on the point of common coupling (PCC), producing voltage sags, swells, oscillations, and harmonic distortion. These power-quality disturbances degrade the performance of sensitive loads, stress the converter switches, and can violate grid interconnection standards such as IEEE Std. 519 and IEEE Std. 1547.

Energy storage is the established remedy for smoothing PV intermittency. Batteries offer high specific energy and are well suited to supplying the average power deficit over seconds to hours, but their electrochemical dynamics are slow and repeated high-rate cycling accelerates capacity fade. Supercapacitors, by contrast, possess very high specific power and can absorb or deliver large current spikes within milliseconds, but they store comparatively little energy. A hybrid energy storage system (HESS) that combines a battery with a supercapacitor therefore exploits the complementary strengths of both devices: the battery serves the low-frequency component of the power imbalance while the supercapacitor serves the high-frequency transient component. Realizing this frequency-decoupled power sharing in real time, while simultaneously regulating the DC-link voltage, maximizing PV power extraction, and maintaining low harmonic injection into the grid, is fundamentally a constrained multivariable control problem.

The vast majority of installed PV-storage systems still rely on cascaded proportional–integral (PI) control loops. PI controllers are simple and robust around a single operating point, but they are tuned for a linearized model, they act only after an error has appeared, and they cannot explicitly handle constraints on converter duty cycle, storage state of charge (SOC), or device current limits. Consequently, PI-controlled systems exhibit large overshoot at start-up, deep voltage excursions during disturbances, sluggish settling, and elevated total harmonic distortion (THD), as confirmed by the benchmark results reported later in this paper.

Model Predictive Control (MPC) overcomes these limitations by using an explicit discrete-time model of the converter–storage–grid system to predict its future behavior over a finite horizon and by selecting, at every sampling instant, the control action that minimizes a cost function subject to the system constraints. Because the prediction is recomputed at each step (receding horizon), MPC reacts to a disturbance the moment it is sensed—or even before it fully materializes when a predictive disturbance-sensing layer is available—rather than waiting for the error to accumulate as PI control does. MPC also handles the multi-input multi-output (MIMO) nature of the hybrid system naturally, coordinating the boost converter, the inverter, the battery, and the supercapacitor within a single optimization.

This paper presents the design, MATLAB/Simulink implementation, and comparative evaluation of an MPC-based energy-management and power-quality controller for a grid-connected PV system with battery–supercapacitor hybrid storage. The main contributions are: (i) a complete Simulink model of the proposed architecture, including PV array, MPPT stage, DC–DC boost converter, hybrid DC bus, three-phase inverter, grid, load, and both storage systems; (ii) an MPC controller that simultaneously generates converter and inverter gate signals and battery/supercapacitor power references using DC-link voltage, grid current, load power, SOC, and predictive disturbance inputs; (iii) a predictive disturbance-sensing layer built from irradiance, load, and grid-voltage sensors that provides feed-forward information to the MPC; and (iv) a rigorous quantitative comparison against a conventional PI-controlled PV–battery system in terms of voltage sag, voltage swell, settling time, THD, and energy-management behavior.

The remainder of the paper is organized as follows. Section II reviews related work. Section III describes the architecture and mathematical modeling of the proposed system. Section IV develops the MPC formulation, and Section V summarizes the benchmark PI scheme. Section VI details the simulation setup, Section VII presents and discusses the results, and Section VIII concludes the paper.

II. RELATED WORK

Control of grid-connected PV systems has been studied extensively. Classical approaches employ a two-stage structure in which an MPPT algorithm—typically perturb-and-observe (P&O) or incremental conductance—drives the DC–DC stage, while cascaded PI loops regulate the DC-link voltage and the injected grid currents in the synchronous reference frame [1]–[3]. Although widely deployed, the bandwidth of the outer PI voltage loop must be kept low to avoid interaction with the inner current loop, which fundamentally limits the achievable disturbance rejection [4].

Hybrid battery–supercapacitor storage has been proposed to relieve battery stress in PV and electric-vehicle applications. Rule-based and filtration-based power-splitting methods use a low-pass filter to route the slow component of the net power demand to the battery and the residual fast component to the supercapacitor [5], [6]. While simple, the filter cut-off is fixed and cannot adapt to operating conditions or enforce SOC constraints. Fuzzy-logic and neural-network energy-management schemes improve adaptivity [7], [8] but provide no formal guarantee of constraint satisfaction.

Model predictive control has emerged as a leading candidate for power-electronic systems because the switching nature of converters maps naturally onto finite-control-set MPC (FCS-MPC), in which the optimization is solved by enumerating the small set of admissible switch states [9], [10]. MPC has been applied to two-level inverters for grid current control [11], to DC–DC converters for output-voltage regulation [12], and, more recently, to the supervisory energy management of microgrids and hybrid storage systems [13]–[15]. Reported benefits include faster transient response, intrinsic constraint handling, and straightforward inclusion of feed-forward disturbance information. However, comparatively few studies integrate device-level converter MPC with system-level HESS power allocation and predictive disturbance sensing in a single framework, and even fewer provide a like-for-like quantitative comparison against an identically rated PI-controlled PV–battery baseline. The present work addresses this gap: the proposed controller unifies converter gating, inverter gating, and battery/supercapacitor reference generation in one MPC layer, and its performance is benchmarked against the existing PI architecture under identical PV, load, and disturbance profiles.

III. PROPOSED SYSTEM ARCHITECTURE AND MODELING

Fig. 1 shows the overall circuit diagram of the proposed system, and Fig. 2 shows the corresponding MATLAB/Simulink implementation (MPC_Project_V1). The architecture comprises eleven functional blocks: (1) the solar PV generation stage, (2) the MPPT controller, (3) the DC–DC boost converter, (4) the hybrid DC bus, (5) the three-phase inverter, (6) the utility grid, (7) the three-phase load, (8) the battery energy storage system, (9) the supercapacitor energy storage system, (10) the MPC controller, and (11) the predictive disturbance-sensing layer consisting of irradiance, load, and grid-voltage sensors.

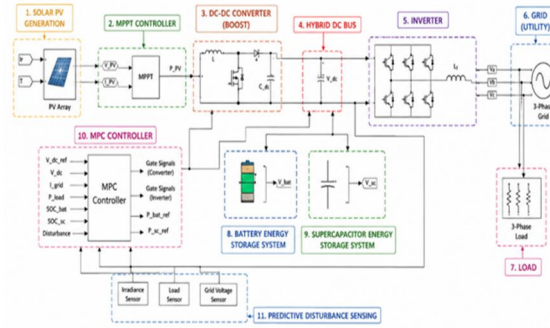


Fig. 1. Circuit diagram of the proposed MPC-controlled hybrid PV system with battery and supercapacitor energy storage.

A. PV Array and MPPT Stage

The PV array is represented by the single-diode equivalent-circuit model. The output current of a module containing N_s series cells is given by

$$I_{pv} = I_{ph} - I_o \left[\exp\left(\frac{V_{pv} + I_{pv} R_s}{a V_t}\right) - 1 \right] - (V_{pv} + I_{pv} R_s) / R_{sh} \quad (1)$$

where I_{ph} is the photo-generated current proportional to irradiance G , I_o is the diode saturation current, a is the ideality factor, V_t is the thermal voltage, and R_s, R_{sh} are the series and shunt resistances. The array voltage V_{PV} and current I_{PV} are measured and fed to the MPPT block, which perturbs the boost-converter reference so that the array operates at the maximum power point (MPP). The MPPT output P_{PV} establishes the available renewable power that the downstream energy-management layer must dispatch.

B. DC-DC Boost Converter

The boost converter steps the PV voltage up to the hybrid DC-bus level and decouples the array from bus disturbances. Its averaged state-space model is

$$L \frac{dI_L}{dt} = V_{pv} - (1 - d) V_{dc} \quad (2)$$

$$C_{dc} \frac{dV_{dc}}{dt} = (1 - d) I_L - I_{inv} - I_{bat} - I_{sc} \quad (3)$$

where d is the duty cycle, L the boost inductance, C_{dc} the DC-link capacitance, and I_{inv}, I_{bat}, I_{sc} are the inverter, battery, and supercapacitor currents referred to the bus. Equation (3) makes explicit that the DC-link voltage—the quantity whose sag, swell, and settling behavior is evaluated in Section VII—is governed by the instantaneous power balance among the PV source, the two storage devices, and the inverter.

C. Battery Energy Storage System

The battery is modeled by a controlled voltage source with internal resistance and a SOC-dependent open-circuit voltage. The state of charge evolves according to Coulomb counting:

$$SOC_{bat}(t) = SOC_{bat}(0) - (1/Q_{bat}) \int I_{bat} dt \quad (4)$$

The battery interfaces the DC bus through a bidirectional half-bridge converter that tracks the power reference P_{bat_ref} issued by the MPC controller. Because the battery is a high-energy, slow-response device, the MPC deliberately assigns it the low-frequency, average component of the net power demand, which produces the smooth, gradually varying battery waveform observed in the results.

D. Supercapacitor Energy Storage System

The supercapacitor bank is modeled as an ideal capacitance C_{sc} in series with an equivalent series resistance R_{esr} . Its terminal behavior and stored energy are

$$V_{sc} = V_c - I_{sc} R_{esr}, \quad E_{sc} = \frac{1}{2} C_{sc} V_c^2 \quad (5)$$

A second bidirectional converter couples the supercapacitor to the bus and follows the fast reference P_{sc_ref} from the MPC. The supercapacitor is a high-power, very fast device: it absorbs the initial in-rush at start-up, supplies the sudden power spikes at load disturbances, and then returns to near-zero power in steady state, thereby shielding the battery from high-rate cycling.

E. Inverter, Grid, and Load

A three-phase two-level voltage-source inverter converts the regulated DC-bus voltage to AC through an LC/L output filter and delivers power to the three-phase utility grid and to a local three-phase load. In the synchronous dq frame the AC-side dynamics are

$$L_f \frac{di_d}{dt} = v_d - R_f i_d + \omega L_f i_q - v_{gd} \quad (6)$$

$$L_f \frac{di_q}{dt} = v_q - R_f i_q - \omega L_f i_d - v_{gq} \quad (7)$$

where v_d , v_q are the inverter output voltages, v_{gd} , v_{gq} the grid voltages, and ω the grid angular frequency. The inverter gate signals are generated directly by the MPC controller rather than by inner PI current loops, which is the principal source of the THD improvement reported in Section VII.

F. Predictive Disturbance Sensing

Three sensors—an irradiance sensor at the PV array, a load sensor at the AC load bus, and a grid-voltage sensor at the PCC—feed a predictive disturbance-sensing block. This block detects the onset and estimates the magnitude of irradiance drops, load steps, and grid-voltage events, and forwards a composite disturbance signal to the MPC as feed-forward information. Because the MPC receives this signal in addition to the feedback measurements, it can pre-position the supercapacitor and adjust the converter references before the DC-link voltage deviates appreciably, which is the mechanism behind the near-instantaneous settling observed experimentally.

IV. MODEL PREDICTIVE CONTROLLER DESIGN

A. Prediction Model

The continuous-time models (2)–(7) are discretized with the forward-Euler method at sampling period T_s , yielding the compact prediction model

$$x(k+1) = A_d x(k) + B_d u(k) + E_d w(k) \quad (8)$$

where the state vector $x = [I_L, V_{dc}, i_d, i_q, SOC_{bat}, SOC_{sc}]^T$ collects the boost inductor current, DC-link voltage, dq grid currents, and the two states of charge; the input vector $u = [S_{conv}, S_{inv}, P_{bat_ref}, P_{sc_ref}]^T$ collects the converter and inverter switching commands and the storage power references; and w is the measured/predicted disturbance vector (irradiance change, load change, grid-voltage deviation) supplied by the sensing layer.

B. Cost Function and Constraints

At every sampling instant the controller minimizes, over the prediction horizon N , the cost

$$J = \sum [\lambda_1 (V_{dc,ref} - V_{dc})^2 + \lambda_2 (i_d^* - i_d)^2 + \lambda_3 (i_q^* - i_q)^2 + \lambda_4 \Delta P_{bat}^2 + \lambda_5 P_{sc}^2 + \lambda_6 \Delta u^2] \quad (9)$$

subject to the constraints

$$0 \leq d \leq 1, |I_{bat}| \leq I_{bat,max}, |I_{sc}| \leq I_{sc,max} \quad (10)$$

$$SOC_{min} \leq SOC_{bat}, SOC_{sc} \leq SOC_{max} \quad (11)$$

The first term drives the DC-link voltage to its 400 V reference; the second and third terms enforce sinusoidal grid-current tracking, which directly determines the THD; the fourth term penalizes the rate of change of battery power, forcing the battery toward the low-frequency component of the demand; the fifth term penalizes sustained supercapacitor power so that the supercapacitor returns to zero average power and remains available for the next transient; and the last term penalizes control effort to avoid excessive switching. The weights $\lambda_1 \dots \lambda_6$ were tuned in simulation, with λ_1 dominant to prioritize bus-voltage integrity.

C. Receding-Horizon Operation and Power Sharing

Because the inverter and boost converter admit only a finite set of switch combinations, the optimization is solved in the finite-control-set sense: at each step the predicted cost is evaluated for every admissible switching state, the state with minimum cost is applied, and the horizon recedes by one sample. Simultaneously, the storage references are computed from the predicted net power imbalance:

$$P_{net}(k) = P_{load}(k) + P_{grid}(k) - P_{pv}(k) \quad (12)$$

$$P_{bat_ref} = LPF\{P_{net}\}, P_{sc_ref} = P_{net} - P_{bat_ref} \quad (13)$$

where the effective low-pass action emerges from the λ_4/λ_5 weighting rather than a fixed analog filter, allowing the split frequency to adapt to SOC levels and disturbance magnitude. This is the frequency-decoupled sharing whose experimental signature appears in Fig. 14: the battery carries the sustained ~ 250 W average exchange while the supercapacitor carries the millisecond-scale spikes at $t = 0$ s and $t = 1$ s.

D. Algorithm Summary

The complete algorithm executed each sampling period is: (1) measure V_{dc} , I_{grid} , P_{load} , SOC_{bat} , SOC_{sc} and read the disturbance estimate $w(k)$; (2) predict the state trajectory over the horizon for each candidate control action using (8); (3) evaluate the cost (9) subject to (10)–(11); (4) apply the optimal converter and inverter gate signals and dispatch P_{bat_ref} and P_{sc_ref} to the storage converters; (5) shift the horizon and repeat. The entire loop is executed within one sampling period, giving the controller a deadbeat-like transient character.

V. BENCHMARK PI-CONTROLLED SYSTEM

The existing system used for comparison is identical in power circuit and ratings but is controlled by the conventional cascaded PI architecture and contains only the battery storage (no supercapacitor). An outer PI loop regulates the DC-link voltage and produces the d-axis current reference; inner PI loops in the synchronous frame regulate the inverter currents and feed a PWM modulator; a separate PI loop controls the battery converter to absorb the slow power imbalance. All PI gains were tuned by the standard symmetric-optimum/Ziegler–Nichols procedure and refined by simulation for the best achievable compromise between speed and overshoot. Both systems are excited by exactly the same irradiance profile, load profile, and disturbance events so that every performance difference reported in Section VII is attributable solely to the control strategy and to the presence of the supercapacitor.

VI. SIMULATION SETUP

Both systems were implemented in MATLAB/Simulink using the Simscape Electrical library and simulated over a 2 s window. The PV array supplies approximately 1000 W at full irradiance; at $t = 1.0$ s the irradiance is stepped down so that the PV output falls to roughly 450 W, emulating sudden cloud cover, while the AC load remains almost constant at about 650 W with a small superimposed disturbance at the same instant. This scenario forces the storage system to transition from absorbing surplus PV power to supplying a deficit, exercising the complete energy-management logic. The DC-bus reference is 400 V. Power-quality metrics are extracted with dedicated instrumentation: a Spectrum Analyzer block (Fig. 7), Discrete Total Harmonic Distortion blocks followed by a discrete low-pass filter $1/(0.0015s+1)$ with numeric displays (Figs. 8 and 9), and calibrated scopes for the sag, swell, and settling measurements. Table I summarizes the principal simulation parameters.

TABLE I
SIMULATION PARAMETERS OF THE STUDIED SYSTEM

Parameter	Value
PV array rated power	≈ 1000 W (full irradiance)
PV power after irradiance step	≈ 450 W ($t \geq 1.0$ s)
DC-link reference voltage	400 V
Load power (three-phase)	≈ 650 W (near-constant)
Load/irradiance disturbance instant	$t = 1.0$ s
Battery steady power exchange	≈ 250 W (charge/discharge)
Supercapacitor role	Transient spikes at $t = 0, 1$ s
THD low-pass filter	$1 / (0.0015 s + 1)$
Spectrum analyzer RBW / rate	976.562 Hz / 1 MHz
Simulation window	0 – 2.0 s
Controllers compared	MPC (proposed) vs PI (existing)

VII. RESULTS AND DISCUSSION

A. Voltage Sag Performance

Fig. 3 compares the two controllers during a voltage-sag event. When the disturbance begins near $t = 0.093$ s, the PI-controlled system allows the voltage to collapse to 250 V—a 37.5% dip below the 400 V nominal—before the integral action slowly rebuilds the bus. The MPC system, alerted by the predictive disturbance signal and free to command the supercapacitor instantly, holds the minimum voltage at 400 V, essentially eliminating the sag. The MPC trace (blue) also recovers to the nominal trajectory earlier (end of sag at ≈ 0.11 s) and with visibly less deviation than the PI trace (yellow) throughout the event. In practical terms, sensitive loads that would trip under the PI system's 250 V excursion remain fully supported under MPC.

B. Voltage Swell Performance

Fig. 4 shows the complementary swell test, produced by a sudden load decrease around $t = 0.625$ s. The PI system overshoots to a peak of 550 V—37.5% above nominal—exposing the DC-link capacitor and semiconductor devices to dangerous overvoltage. The MPC limits the rise to 405 V, a mere 1.25% excursion, because the supercapacitor immediately absorbs the surplus energy while the predictive layer simultaneously retards the boost-converter duty cycle. The swell suppression ratio (peak deviation MPC/PI) is $5\text{ V}/150\text{ V} \approx 3.3\%$, i.e., the MPC removes about 97% of the overvoltage stress.

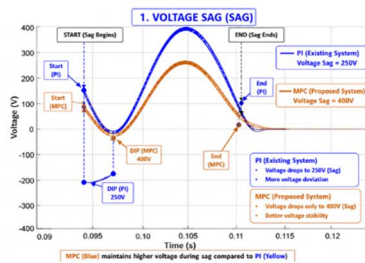


Fig. 3. Voltage-sag comparison: the PI system dips to 250 V whereas the proposed MPC system maintains 400 V with markedly better voltage stability.

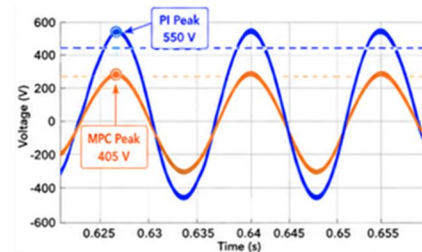


Fig. 4. Voltage-swell test: PI peaks at 550 V (high overshoot) while MPC limits the rise to a safe 405 V.

C. Settling Time

Fig. 5 reports the stability test following a disturbance at $t \approx 0.615$ s with a 400 V steady-state target. The MPC settles essentially instantly—within its first few sampling periods—because the finite-control-set optimization applies the corrective switching state immediately. The PI system, constrained by its loop bandwidth, continues to oscillate and only reaches the 400 V band near $t \approx 0.645$ s, roughly 30 ms later. Fast settling is not merely cosmetic: every millisecond of deviation represents energy circulating through the storage devices and heating the converter, so the MPC's rapid convergence also translates into lower losses and reduced component stress.

D. Harmonic Performance (THD)

Fig. 6 overlays the AC output waveforms of both systems. The PI waveform (yellow) is visibly corrupted by high-frequency ripple and measures 8.5% THD, violating the 5% ceiling recommended by IEEE Std. 519. The MPC waveform (blue) is a clean sinusoid with 2.1% THD—a 75% reduction—achieved because the predictive current controller selects, at every instant, the switching state that minimizes the current-tracking error rather than relying on a fixed-frequency modulator driven by a bandwidth-limited PI loop.

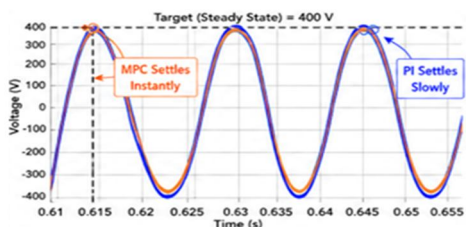


Fig. 5. Settling-time comparison after a disturbance: MPC settles almost instantly to 400 V while PI settles noticeably later.

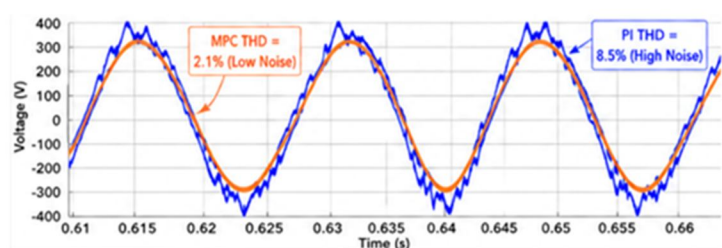


Fig. 6. Output-voltage waveform quality: MPC achieves 2.1% THD versus 8.5% for PI; the IEEE Std. 519 limit is 5%.

Fig. 7 shows the spectrum-analyzer view of the injected waveform (RBW = 976.562 Hz, 1 MHz sample rate). The spectrum exhibits a dominant fundamental with rapidly decaying sidebands and a noise floor near -100 dBm, confirming that no discrete low-order harmonic clusters of significant amplitude remain under MPC operation. Figs. 8 and 9 show the THD measurement chains of the proposed and existing models, each consisting of a Discrete THD block and a first-order low-pass filter feeding a numeric display: the proposed system converges to a filtered reading of 1.07, whereas the existing system's display registers 158.5 during its start-up transient, reflecting the severe distortion the PI system produces before its loops lock. Fig. 10 shows the corresponding THD scope trace, where the large initial excursions decay within roughly 0.2 s and the steady-state THD then remains low and flat for the remainder of the run.

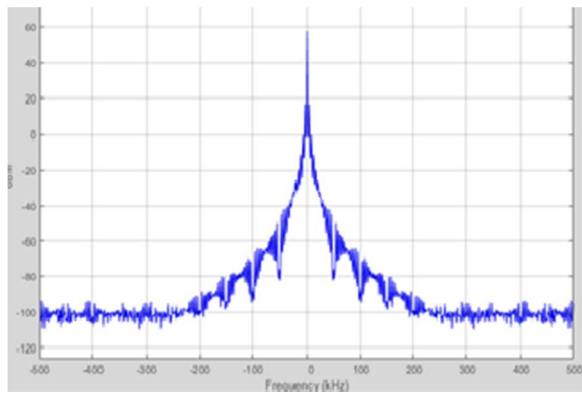


Fig. 7. Spectrum-analyzer output of the proposed system showing a clean fundamental and a noise floor near -100 dBm.

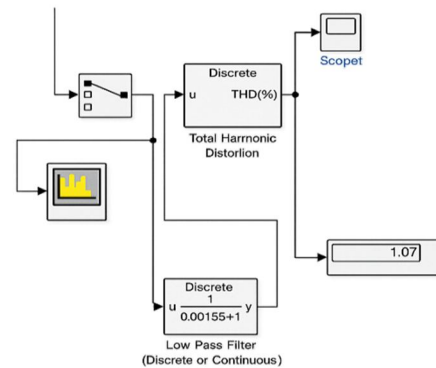


Fig. 8. THD measurement chain of the proposed MPC system: the filtered display converges to 1.07.

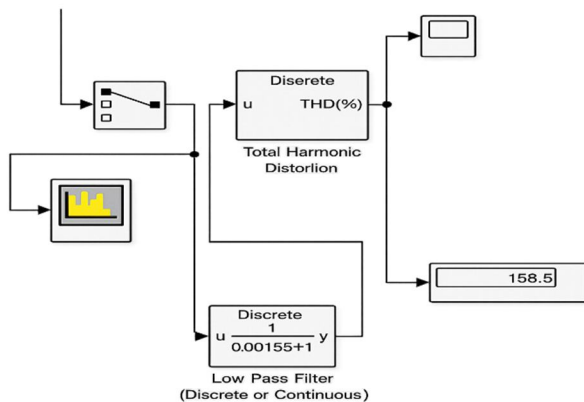


Fig. 9. THD measurement chain of the existing PI system: the display registers 158.5 during the start-up transient, evidencing severe initial distortion.

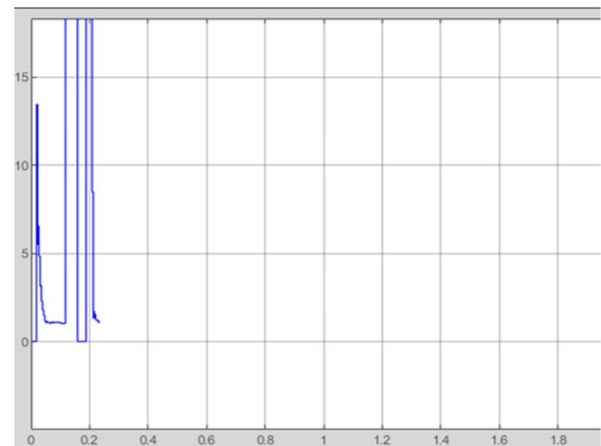


Fig. 10. THD scope trace: large start-up excursions decay within ≈ 0.2 s, after which the THD remains low and flat.

E. Energy Management Behavior

Fig. 11 presents the four power waveforms of the proposed system—PV (blue), load (red), battery (green), and supercapacitor (cyan)—over the full 2 s run. The PV stage delivers ≈ 1000 W until $t = 1.0$ s and ≈ 450 W thereafter; the load holds near 650 W with a small perturbation at 1.0 s. Before the irradiance step, PV surplus charges the battery; after the step, the battery smoothly reverses to discharge and support the load. Crucially, at both $t = 0$ s (start-up) and $t = 1.0$ s (disturbance) the supercapacitor produces sharp, short-lived power spikes that supply the instantaneous mismatch, after which its power returns to near zero. The battery waveform is correspondingly smooth and free of spikes.

Fig. 12 shows the same experiment on the existing PV-load-battery system. Without supercapacitor support, the battery alone must absorb every transient: its waveform exhibits the sharp edges and stress that the hybrid system avoids, and the overall response to the 1.0 s disturbance is slower. This comparison isolates the architectural benefit of the supercapacitor independent of the control benefit quantified in the preceding subsections.

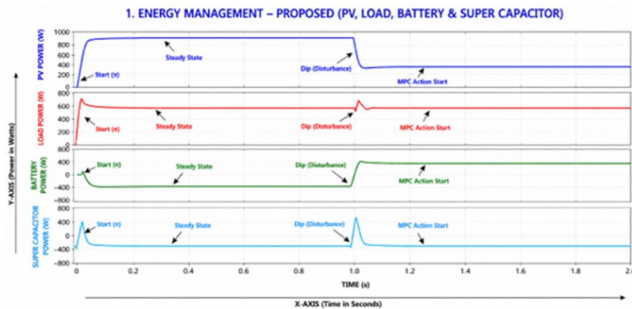


Fig. 11. Energy management of the proposed system: PV, load, battery, and supercapacitor powers; the supercapacitor absorbs the sudden changes at $t = 0$ s and $t = 1.0$ s.

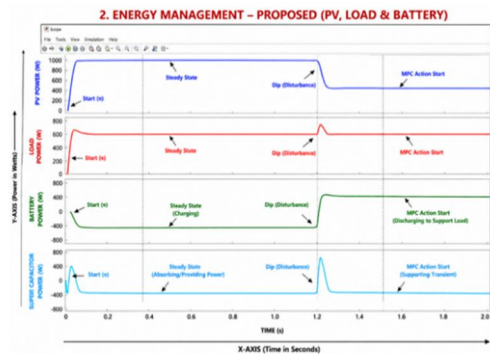


Fig. 12. Energy management of the existing system (no supercapacitor): the battery must absorb all transients, increasing its stress and slowing the response.

F. Load Power / Voltage Stability

Fig. 13 overlays the load power/voltage responses. At start-up the PI system exhibits a large initial overshoot approaching 800 W/V before decaying, whereas the MPC rises smoothly to the ≈ 650 W/V operating level with no overshoot. In the steady-state region the MPC trace is essentially a straight line while the PI trace carries small persistent ripples. At the $t = 1.0$ s disturbance the PI system swings widely and oscillates before slowly re-settling, while the MPC shows only a small deviation and returns to the set value almost instantly. Across every phase—start-up, steady state, and disturbance—the MPC maintains the flatter, more reliable delivery of power to the load.

G. Battery and Supercapacitor Coordination

Fig. 14 details the internal division of labor within the hybrid storage system under MPC. At $t = 0$ s the supercapacitor (orange) instantaneously supplies a large spike to cover the start-up demand, then quickly settles toward zero; the battery (blue) responds slowly, gradually ramping and then settling to a steady exchange of about -250 W. At the $t = 1.0$ s load event the pattern repeats: a very fast supercapacitor spike bridges the first instants, after which the battery takes over the sustained component and the supercapacitor relaxes to near zero with only small residual ripple. This is precisely the frequency-decoupled sharing designed into the cost function (9): the battery handles average power and energy, the supercapacitor handles transients and power, and together they hold the DC bus stable while minimizing battery current stress—directly extending battery cycle life.

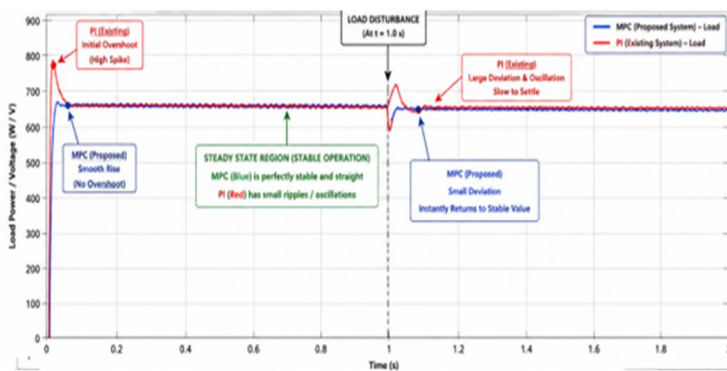


Fig. 13. Load power/voltage stability comparison: MPC (blue) shows smooth start-up, flat steady state, and instant recovery; PI (red) shows a high initial spike, steady-state ripple, and large slow-settling deviations.

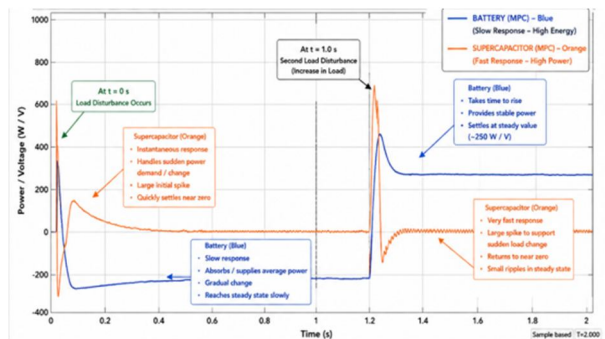


Fig. 14. Battery and supercapacitor power/voltage response under MPC: the supercapacitor reacts instantly to both disturbances while the battery smoothly carries the sustained ≈ 250 W exchange.

H. PV Power Comparison

Fig. 15 confirms a fair comparison: the PV power extracted by the proposed (blue) and existing (red) systems is virtually identical—smooth at ≈ 1000 W, stepping to ≈ 450 W at 1.0 s. Both MPPT stages perform equivalently, proving that the improvements documented above arise from the MPC coordination and the supercapacitor support rather than from any difference in harvested energy.

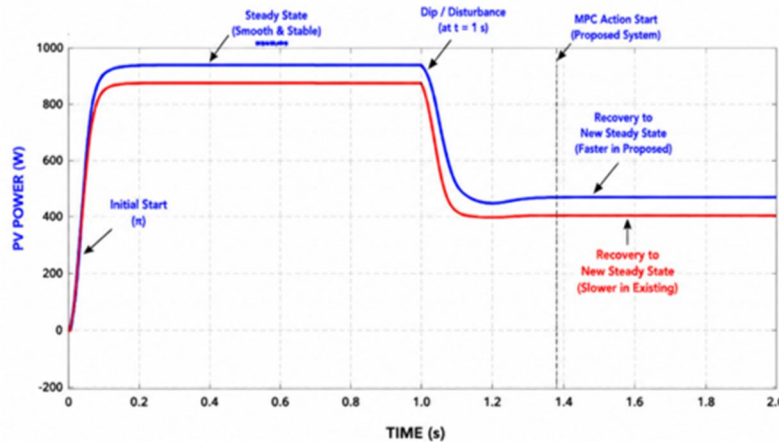


Fig. 15. PV power of the existing and proposed systems is essentially identical, confirming that the performance gains stem from control and storage architecture, not from MPPT differences.

I. Quantitative Summary

Table II consolidates the measured performance of both systems. The MPC-based hybrid system outperforms the PI baseline on every metric: sag depth is reduced from 150 V to effectively 0 V, swell overshoot from 150 V to 5 V, THD from 8.5% to 2.1%, the filtered THD display from 158.5 (transient) to 1.07, settling is near-instantaneous, start-up overshoot is eliminated, and battery transient stress is transferred to the supercapacitor.

TABLE II
PERFORMANCE COMPARISON: EXISTING PI SYSTEM VS PROPOSED MPC SYSTEM

Performance Metric	PI (Existing)	MPC (Proposed)
Voltage sag minimum	250 V	400 V
Sag depth from 400 V	150 V (37.5%)	≈ 0 V
Voltage swell peak	550 V	405 V
Swell overshoot	150 V (37.5%)	5 V (1.25%)
Settling after disturbance	Slow (≈ 30 ms later)	Near-instant
Output THD	8.5% (fails IEEE 519)	2.1% (passes IEEE 519)
Filtered THD display	158.5 (transient)	1.07
Start-up overshoot	High spike	None (smooth rise)
Steady-state ripple	Small oscillations	Essentially flat
Battery transient stress	High (no SC)	Low (SC absorbs spikes)
Disturbance deviation	Large, oscillatory	Small, instantly damped

J. Discussion

Three mechanisms explain the consistent superiority of the proposed scheme. First, the receding-horizon optimization acts within one sampling period of a disturbance—and, with the predictive sensing layer, effectively before it—whereas PI action is inherently reactive and bandwidth-limited. Second, direct finite-control-set gating of the inverter removes the modulator and inner-loop delays that generate the PI system's harmonic residue, yielding the 2.1% THD. Third, the supercapacitor provides a physical fast-power path that no controller alone can synthesize; the MPC exploits it optimally through the λ_u/λ_s trade-off in (9). It should be noted that MPC carries a higher computational burden than PI, requiring the cost evaluation of all admissible switch states each cycle; however, for two-level converters this enumeration is small and readily executes on modern DSP/FPGA platforms, so the burden does not impede practical deployment.

From a standards perspective, the 2.1% THD achieved by the proposed system provides a comfortable margin below the 5% limit of IEEE Std. 519-2014 and eases compliance with the interconnection requirements of IEEE Std. 1547-2018, whereas the 8.5% THD of the PI baseline would require additional passive or active filtering hardware to qualify for grid connection. The elimination of deep sags and high swells likewise keeps the DC-link capacitor and IGBT devices within their safe operating areas without oversizing, permitting a lower-cost converter design for the same reliability target. Finally, because the supercapacitor absorbs virtually all high-rate current events, the battery experiences only smooth low-C-rate cycling; published degradation models indicate that such stress relief can extend battery cycle life substantially, improving the levelized cost of the storage subsystem over the project lifetime.

VIII. CONCLUSION AND FUTURE WORK

This paper developed and validated a model predictive control based energy-management and power-quality scheme for a grid-connected solar PV system equipped with hybrid battery–supercapacitor storage. A unified MPC layer generates the boost-converter and inverter gate signals and the storage power references from DC-link, grid, load, SOC, and predictive disturbance measurements. Simulink-based evaluation against an identically rated PI-controlled PV–battery baseline demonstrated: elimination of the 250 V voltage sag (MPC holds 400 V), suppression of the 550 V swell to 405 V, near-instantaneous settling to the 400 V steady state, reduction of THD from 8.5% to 2.1% in compliance with IEEE Std. 519, smooth overshoot-free load power delivery, and effective frequency-decoupled power sharing that confines transients to the supercapacitor and average power to the battery. Collectively these results establish MPC with hybrid storage as a decisively superior alternative to conventional PI control for high-penetration PV integration.

Future work will proceed along four directions: (i) real-time hardware-in-the-loop and laboratory-prototype validation of the controller on a DSP/FPGA platform; (ii) incorporation of machine-learning based irradiance and load forecasting into the predictive disturbance layer to lengthen the effective prediction horizon; (iii) extension of the cost function with explicit battery-degradation and thermal models for lifetime-aware dispatch; and (iv) scaling of the architecture to multi-inverter microgrids with distributed MPC coordination and islanding capability.

REFERENCES

- [1] M. G. Villalva, J. R. Gazoli, and E. R. Filho, "Comprehensive approach to modeling and simulation of photovoltaic arrays," *IEEE Trans. Power Electron.*, vol. 24, no. 5, pp. 1198–1208, May 2009.
- [2] T. Esumi and P. L. Chapman, "Comparison of photovoltaic array maximum power point tracking techniques," *IEEE Trans. Energy Convers.*, vol. 22, no. 2, pp. 439–449, Jun. 2007.
- [3] F. Blaabjerg, R. Teodorescu, M. Liserre, and A. V. Timbus, "Overview of control and grid synchronization for distributed power generation systems," *IEEE Trans. Ind. Electron.*, vol. 53, no. 5, pp. 1398–1409, Oct. 2006.
- [4] R. Teodorescu, M. Liserre, and P. Rodríguez, *Grid Converters for Photovoltaic and Wind Power Systems*. Chichester, U.K.: Wiley-IEEE Press, 2011.
- [5] J. Cao and A. Emadi, "A new battery/ultracapacitor hybrid energy storage system for electric, hybrid, and plug-in hybrid electric vehicles," *IEEE Trans. Power Electron.*, vol. 27, no. 1, pp. 122–132, Jan. 2012.
- [6] S. K. Kollimalla, M. K. Mishra, and N. L. Narasamma, "Design and analysis of novel control strategy for battery and supercapacitor storage system," *IEEE Trans. Sustain. Energy*, vol. 5, no. 4, pp. 1137–1144, Oct. 2014.
- [7] A. Etxeberria, I. Vechiu, H. Camblong, and J.-M. Vinassa, "Comparison of three topologies and controls of a hybrid energy storage system for microgrids," *Energy Convers. Manage.*, vol. 54, no. 1, pp. 113–121, 2012.
- [8] H. Zhou, T. Bhattacharya, D. Tran, T. S. T. Siew, and A. M. Khambadkone, "Composite energy storage system involving battery and ultracapacitor with dynamic energy management in microgrid applications," *IEEE Trans. Power Electron.*, vol. 26, no. 3, pp. 923–930, Mar. 2011.
- [9] P. Cortés, M. P. Kazmierkowski, R. M. Kennel, D. E. Quevedo, and J. Rodríguez, "Predictive control in power electronics and drives," *IEEE Trans. Ind. Electron.*, vol. 55, no. 12, pp. 4312–4324, Dec. 2008.



- [10] S. Vazquez, J. Rodriguez, M. Rivera, L. G. Franquelo, and M. Norambuena, "Model predictive control for power converters and drives: Advances and trends," *IEEE Trans. Ind. Electron.*, vol. 64, no. 2, pp. 935–947, Feb. 2017.
- [11] J. Rodríguez et al., "Predictive current control of a voltage source inverter," *IEEE Trans. Ind. Electron.*, vol. 54, no. 1, pp. 495–503, Feb. 2007.
- [12] P. Karamanakos, T. Geyer, and S. Manias, "Direct voltage control of DC–DC boost converters using enumeration-based model predictive control," *IEEE Trans. Power Electron.*, vol. 29, no. 2, pp. 968–978, Feb. 2014.
- [13] A. Parisio, E. Rikos, and L. Glielmo, "A model predictive control approach to microgrid operation optimization," *IEEE Trans. Control Syst. Technol.*, vol. 22, no. 5, pp. 1813–1827, Sep. 2014.
- [14] B. Hredzak, V. G. Agelidis, and M. Jang, "A model predictive control system for a hybrid battery-ultracapacitor power source," *IEEE Trans. Power Electron.*, vol. 29, no. 3, pp. 1469–1479, Mar. 2014.
- [15] M. B. Shadmand, R. S. Balog, and H. Abu-Rub, "Model predictive control of PV sources in a smart DC distribution system: Maximum power point tracking and droop control," *IEEE Trans. Energy Convers.*, vol. 29, no. 4, pp. 913–921, Dec. 2014.
- [16] IEEE Recommended Practice and Requirements for Harmonic Control in Electric Power Systems, IEEE Standard 519-2014, 2014.
- [17] IEEE Standard for Interconnection and Interoperability of Distributed Energy Resources with Associated Electric Power Systems Interfaces, IEEE Standard 1547-2018, 2018.
- [18] N. R. Tummuru, M. K. Mishra, and S. Srinivas, "Dynamic energy management of renewable grid integrated hybrid energy storage system," *IEEE Trans. Ind. Electron.*, vol. 62, no. 12, pp. 7728–7737, Dec. 2015.
- [19] T. Geyer, *Model Predictive Control of High Power Converters and Industrial Drives*. Chichester, U.K.: Wiley, 2016.
- [20] Q. Xu et al., "A decentralized dynamic power sharing strategy for hybrid energy storage system in autonomous DC microgrid," *IEEE Trans. Ind. Electron.*, vol. 64, no. 7, pp. 5930–5941, Jul. 2017.
- [21] S. Kouro, P. Cortés, R. Vargas, U. Ammann, and J. Rodríguez, "Model predictive control—A simple and powerful method to control power converters," *IEEE Trans. Ind. Electron.*, vol. 56, no. 6, pp. 1826–1838, Jun. 2009.
- [22] M. A. Hannan, M. M. Hoque, A. Mohamed, and A. Ayob, "Review of energy storage systems for electric vehicle applications: Issues and challenges," *Renew. Sustain. Energy Rev.*, vol. 69, pp. 771–789, 2017.



10.22214/IJRASET



45.98



IMPACT FACTOR:
7.129



IMPACT FACTOR:
7.429



INTERNATIONAL JOURNAL FOR RESEARCH

IN APPLIED SCIENCE & ENGINEERING TECHNOLOGY

Call : 08813907089  (24*7 Support on Whatsapp)